A Parametric Model for Synthetic Aperture Radar Measurements

Michael J. Gerry, Lee C. Potter, *Senior Member, IEEE*, Inder J. Gupta, *Senior Member, IEEE*, and Andria van der Merwe

Abstract—**We present a parametric model for radar scattering as a function of frequency and aspect angle. The model is used for analysis of synthetic aperture radar measurements. The estimated parameters provide a concise, physically relevant description of measured scattering for use in target recognition, data compression and scattering studies. The scattering model and an image domain estimation algorithm are applied to two measured data examples.**

Index Terms—**Image resolution, inverse scattering, radar imaging.**

I. Introduction

At high frequencies, the scattering response of an object is well approximated as a sum of responses from individual scattering centers [1]. These scatterers provide a physically relevant, yet concise, description of the object and are thus good candidates for use in target recognition, radar data compression, and scattering phenomenology. In this paper we consider the analysis of radar data measured as a function of frequency and aspect angle. We develop a parametric scattering model for this two-dimensional (2-D) problem. The model is motivated by both the physical optics and the geometric theory of diffraction (GTD) monostatic scattering solutions and extends the one-dimensional GTD-based parametric model presented in [2] to include aspect angle. Our model provides a physical description of target scattering centers, each of which is described by a set of parameters characterizing position, shape, orientation (pose), and relative amplitude. This is a richer description of target scattering than is available either from conventional Fourier-based imaging techniques [3] or from less physically accurate point scattering parametric models.

Recent developments in mechanism extraction from 2-D radar data [4]–[9] are based on the assumption that scattering centers are localized to isolated points. While this description is valid for many scattering centers at many aspect angles, some common scattering mechanisms behave as distributed elements, and point scattering models fail to accurately model the scattering. The aspect dependence in our 2-D model allows description of both localized and distributed scattering centers, providing a higher fidelity description of scattered fields. The model provides the potential both for improved data compression and for the discrimination of localized versus distributed scattering mechanisms.

The paper is organized as follows. In Section II, we develop a simple parametric model of far-field scattering as a function of frequency and aspect angle. In Section III, we transform the frequency-aspect angle-domain model into the image domain for the purpose of parameter estimation; image segmentation provides the advantages of clutter suppression, model-order reduction, and computational savings. In Section IV, we present an algorithm for estimation of the unknown parameters of the model from an image-domain representation of the measured data. In Section V, we present experimental results obtained by applying our estimation algorithm to data measured in a compact-range anechoic chamber. In Section VI, we use the Cramér–Rao lower bound (CRB) to predict uncertainty in the estimated model parameters.

II. Model Development

We develop a parametric model for the backscatter from objects measured as a function of frequency and aspect angle. We seek a model that maintains high fidelity to the scattering physics for many objects, yet is sufficiently simple in its functional form to permit robust inference from estimated parameters.

For this development, we assume a data collection scenario consistent with synthetic aperture radar (SAR) imaging. A reference point is defined, and we require that the radar trajectory and reference point are coplanar. We label this imaging plane using an x-y Cartesian coordinate system with origin at the reference point. The radar position is then described by an angle ϕ defined counterclockwise from the x direction. We assume far-zone backscatter and, therefore, obtain plane wave incidence on objects.

From the GTD [1] and its uniform version [10], if the wavelength of the incident excitation is small relative to the target extent, then the backscattered field from an object consists of contributions from electrically isolated scattering centers. In developing our model, we characterize the frequency and aspect angle dependence of individual scattering centers. Each scattering center is described by a small number of parameters. The total scattered field from a target is then modeled as the sum of these individual scatterers.

Manuscript received May 2, 1997; revised April 22, 1998. This work was supported by the Defense Advanced Research Projects Agency under Subcontract 348608SC to the Environmental Research Institute of Michigan.

M. J. Gerry was with the ElectroScience Laboratory, Department of Electrical Engineering, The Ohio State University, Columbus, OH 43212 USA. He is now with the Synsis Corporation, DeWitt, NY 13214 USA.

L. C. Potter is with the Department of Electrical Engineering, The Ohio State University, Columbus, OH 43210 USA.

I. J. Gupta and A. van der Merwe are with the ElectroScience Laboratory, Department of Electrical Engineering, The Ohio State University, Columbus, OH 43212 USA.

Publisher Item Identifier S 0018-926X(99)07060-X.

TABLE I
ALPHA VALUES FOR CANONICAL SCATTERERS

α	Example scattering geometries
1	flat plate at broadside; dihedral
$\frac{1}{2}$	singly curved surface reflection
0	point; sphere; straight edge specular
$-\frac{1}{2}$	edge diffraction
-1	corner diffraction

We make three assumptions about the far zone backscattered field and each assumption leads to the functional form for a portion of our scattering model. First, phase dependence is linear and defined by the position of the scattering center. Second, amplitude dependence on frequency is defined by the high-frequency approximation derived from the GTD. Third, amplitude dependence on aspect angle is defined by characterizing the scattering center as either spatially localized or distributed. We consider these three dependencies, each in turn, to arrive at a parametric scattering model.

First, we consider only far-field scattering with a linear phase dependence on frequency. The phase of a scattering center, at a given aspect angle, is determined by the down range position of the scatterer. Accordingly, the backscattered field of the nth scattering center is expressed

$$E_n^s(k,\phi) = S_n(k,\phi)\exp\{j2k\hat{r}\cdot\vec{r}_n\} \tag{1}$$

where $k = 2\pi f/c$ is the wave number, f is frequency in hertz, c is the propagation velocity, ϕ is the aspect angle, $\hat{r}$ is the unit vector in the direction of the scattered field, and $\vec{r}_n = [x_n, y_n]$ is the position vector of the nth scattering center projected to the plane. Note that the restriction to linear phase scatterers excludes phase dispersive scattering mechanisms such as resonant cavities and creeping waves. The $e^{j2\pi ft}$ time convention is assumed and suppressed. Here we consider only the copolarized field; as such, all field quantities are written as scalars. The development is easily extendible to multiple polarizations. In summary, the phase dependence of our model describes the location of each scattering center in the plane of the radar measurement.

Second, we consider the amplitude dependence on frequency. In presenting the GTD, Keller [1] uses a conservation of energy argument to propose that the field diffracted from a point on an edge is proportional to $(jk)^{-\frac{1}{2}}$, and the field diffracted from a vertex is proportional to $(jk)^{-1}$. The simplicity of the GTD is that many practical object geometries give rise to a sum of these two scattering mechanisms. In [11] and [12], it is shown that in addition to the edge and vertex diffraction, a larger class of scattering geometries also fits the $(jk)^{\alpha}$ power dependence on frequency, where the parameter α has a half integer value (see Table I).

Third, we consider aspect dependence of scattering amplitude. As aspect angle is varied, we assume that a scattering center behaves in one of two ways: either a scatterer is localized and appears to exist at a single point in space, or it is distributed in the imaging plane and appears as a finite, nonzero-length current distribution. The amplitude dependence on aspect angle is different for each of these scenarios, and we seek a model that accounts for both scattering behaviors in a physically accurate, yet simple, functional form.

Examples of localized scattering mechanisms are trihedral reflection, corner diffraction, and edge diffraction. All of these mechanisms have slowly varying amplitude as a function of aspect angle. We exploit the commonality of localized mechanisms by modeling this slowly varying function with a damped exponential

$$S_n(f,\phi) = A_n\exp(-2\pi f\gamma_n\sin\phi). \tag{2}$$

The exponential function provides a mathematically convenient approximation containing only a single parameter. Although physical insight is used to arrive at the exponential model, the parameter γ_n has no direct physical interpretation.

On the other hand, examples of distributed scattering mechanisms are flat-plate reflection, dihedral reflection, and cylinder reflection. Each of these scattering mechanisms has an amplitude dependence on aspect angle that contains a $\text{sinc}(x) = \frac{\sin(x)}{x}$ function. In all cases, this $\text{sinc}(x)$ function is the dominant term in the physical optics far-zone scattering solution and we adopt the $\text{sinc}(x)$ function to characterize angle dependence in the scattering model for scattering centers that are distributed

$$S_n(f,\phi) = A_n\ \text{sinc}\left(\frac{2\pi f}{c}L_n\sin(\phi-\bar{\phi}_n)\right) \tag{3}$$

where L_n is the length and $\bar{\phi}_n$ is the orientation angle of the distributed scatterer.

We combine the different model terms from the localized and the distributed scattering mechanisms to write our 2-D scattering model in a single expression

$$\begin{aligned} E_n^s(f,\phi) = {} & A_n\left(j\frac{f}{f_c}\right)^{\alpha_n}\text{sinc}\left(\frac{2\pi f}{c}L_n\sin(\phi-\bar{\phi}_n)\right) \\ & \times\exp(-2\pi f\gamma_n\sin\phi) \\ & \cdot\exp\left(j\frac{4\pi f}{c}(x_n\cos\phi + y_n\sin\phi)\right) \end{aligned} \tag{4}$$

where $L_n = 0$ if the scattering center is localized, and $\gamma_n = 0$ if the scatterer is distributed. The parameter A_n is a relative amplitude for each scattering center. The total scattered field is a sum of p individual scattering terms

$$E^s(f,\phi) = \sum_{n=1}^{p} E_n^s(f,\phi). \tag{5}$$

The scattering model in (4) is a function of frequency and aspect angle and is described by the parameter set $(A_n, x_n, y_n, \alpha_n, \gamma_n, L_n, \bar{\phi}_n)$ for $n = 1,\cdots,p$. The parameters provide a rich physical description of the scatterers that are present in the data set. Each parameter, with the exception of γ_n, has a direct physical interpretation. Example scattering geometries distinguishable by their (α, L) parameters are presented in Table II. The model is based on scattering physics and is developed to describe a large class of scatterers while still maintaining a relatively simple form.

TABLE II
PARAMETERS α AND L SERVE TO DISCRIMINATE MANY SCATTERING GEOMETRIES

Example scattering geometries	α	L
dihedral	1	$L \neq 0$
corner reflector	1	0
cylinder	$\frac{1}{2}$	$L \neq 0$
sphere	0	0
edge broadside	0	$L \neq 0$
corner diffraction	-1	0
double corner diffraction	-2	0

III. Transformation of Model into Image Domain

The model in (4) describes scattering in the frequency-aspect domain. For most SAR data collection geometries, imaging is approximately a unitary operator; therefore, the nonlinear least-squares estimation cost surface for estimating model parameters is essentially the same in either the frequency-aspect domain or the image domain. However, image-domain segmentation provides several practical advantages for computing estimates of the unknown model parameters [4]. The advantages of segmentation are reduction in local model order, clutter suppression, and reduction in computation cost. After segmentation, estimation of parameters directly using image data is computationally convenient; we avoid the additional transformation to the frequency-aspect domain and bypass the frequency-aspect convolution caused by the image segmentation window.

In order to accomplish image domain parameter estimation, we analytically transform the scattering model from the frequency-aspect domain into the image domain. We process the parametric model using the same series of operations through which the motion-compensated frequency-aspect angle measurements would pass during image formation. There are many methods for image formation [3], but we limit the discussion in this work to the 2-D inverse Fourier transform (IFT) of the measured frequency-aspect data. This imaging algorithm is widely used in spotlight SAR systems for which the center frequency of the radar is large compared to the bandwidth of the radar. Accordingly, we analytically perform a 2-D IFT on the proposed frequency-aspect domain scattering model.

We begin with the model in (4) and arrive to an image domain model in four steps. First, we replace the power dependence of amplitude on frequency with an exponential (as in [13])

$$\left(\frac{2\pi f}{c}\right)^{\alpha_n} \approx \exp(-2\pi r_n f) \tag{6}$$

where r_n is a damping factor. We let the j^α term be absorbed into the complex amplitude A_n. We adopt the following affine map from r_n to α_n, as proposed in [13]:

$$\alpha_n = \frac{f_c}{\Delta f}\{\exp(-2\pi \Delta f r_n) - 1\} \tag{7}$$

where f_c is the center frequency, and Δf is the frequency increment. The expression in (7), while analytically convenient, is nonetheless extremely accurate for small relative bandwidths [13]. For example, at 10% relative bandwidth the approximation has less than 0.0001% relative error. As the bandwidth increases this error increases. Using this approximation, we first estimate r_n and then map r_n to α_n.

Second, we translate the model from polar coordinates to Cartesian coordinates via the substitution

$$\begin{aligned} f_x &= f\cos\phi \\ f_y &= f\sin\phi. \end{aligned} \tag{8}$$

By making this coordinate transformation to the Cartesian frequency plane, we assume that the measured data is sufficiently narrow in bandwidth so as to allow simple, approximate interpolation [14], [15] to a rectangular grid. We further approximate

$$2\pi f r_n \approx 2\pi f_x r_n \tag{9}$$

in the frequency-dependent exponential of (6); this approximation is valid for small angle spans.

Third, frequency and angle domain window functions are often used in SAR imaging for sidelobe suppression. We assume that the window functions are separable in their Cartesian components and can be written as

$$\begin{aligned} W(f_x, f_y) &= W_x(f_x)W_y(f_y) \\ W_x(f_x) &= \sum_{p=1}^{P} B_p^x \exp\left(j2\pi\beta_p^x f_x\right) \\ W_y(f_y) &= \sum_{q=1}^{Q} B_q^y \exp\left(j2\pi\beta_q^y f_y\right). \end{aligned} \tag{10}$$

Many commonly used window functions such as rectangular, Hamming, and Taylor windows can be exactly written as in (10).

Fourth, we transform $E_n^s(f_x, f_y)$ to the image domain with a 2-D IFT. Note that, in practice, measured data exists at a finite number of discrete frequencies and aspect angles. As a result, the IFT performed to generate radar imagery is typically an Inverse Discrete Fourier Transform (IDFT). Here we analytically perform a continuous IFT for simplicity. In fact, the alternative image domain model using the IDFT is not available in closed form. The IDFT is approximately equal to the continuous IFT when the image-domain signal is essentially support limited. Since most radar imagery contains a small number of high-energy regions that are limited in extent, the sampling-induced aliasing is negligible. Thus, we assume that the sampled IDFT is well-approximated by a continuous IFT for radar imagery.

The image-domain model $e_n^s(t_x, t_y)$ for a single scattering center is then written as

$$\begin{aligned} e_n^s(t_x, t_y) &= \int_{f_{y1}}^{f_{y2}} \int_{f_{x1}}^{f_{x2}} \Bigg\{ \sum_{p=1}^{P}\sum_{q=1}^{Q} A_n B_p^x B_q^y \\ &\quad \cdot \operatorname{sinc}\left[\frac{2\pi L\cos\bar{\phi}_n}{c}(f_y - f_x\tan\bar{\phi}_n)\right] \\ &\quad \cdot \exp\left[2\pi f_y\left(-\gamma_n + j\left(\frac{2y_n}{c} + \beta_q^y + t_y\right)\right)\right] \\ &\quad \cdot \exp\left[2\pi f_x\left(-r_n + j\left(\frac{2x_n}{c} + \beta_p^x + t_x\right)\right)\right] df_x\, df_y \Bigg\} \end{aligned} \tag{11}$$

where f_{x1}, f_{x2} are the first and last f_x frequencies, and f_{y1}, f_{y2} are the first and last f_y frequencies.

As discussed in Section II, either $L_n = 0$ or $\gamma_n = 0$ and we consider each case separately. If $L_n = 0$, evaluation of the integrals in (11) yields [16]

$$\begin{aligned} c_n^s(t_x, t_y) = A_n \sum_{p=1}^{P} \sum_{q=1}^{Q} B_p^x B_q^y F_x F_y \\ \cdot \exp\left(2\pi f_{xc}\left(-r_n + j\left(\frac{2x_n}{c} + \beta_p^x + t_x\right)\right)\right) \\ \cdot \exp\left(2\pi f_{yc}\left(-\gamma_n + j\left(\frac{2y_n}{c} + \beta_q^y + t_y\right)\right)\right) \\ \cdot \operatorname{sinhc}\left(\pi F_x\left(-r_n + j\left(\frac{2x_n}{c} + \beta_p^x + t_x\right)\right)\right) \\ \cdot \operatorname{sinhc}\left(\pi F_y\left(-\gamma_n + j\left(\frac{2y_n}{c} + \beta_q^y + t_y\right)\right)\right) \end{aligned} \tag{12}$$

where

$$\begin{aligned} F_x &= f_{x2} - f_{x1} \\ F_y &= f_{y2} - f_{y1} \\ f_{xc} &= \frac{f_{x2} + f_{x1}}{2} \\ f_{yc} &= \frac{f_{y2} + f_{y1}}{2} \\ \operatorname{sinhc}(x) &= \frac{\sinh(x)}{x}. \end{aligned}$$

The model in (12) is for $L = 0$, which corresponds to a localized scattering mechanism. In the image domain, the localized mechanism is represented by two separable functions in t_x and t_y, each of which appears as a $\operatorname{sinhc}(x)$ function.

On the other hand, if $\gamma_n = 0$, then evaluation of the integrals in (11) yields [16]

$$\begin{aligned} c_n^s(t_x, t_y) = A_n \sum_{p=1}^{P} \sum_{q=1}^{Q} B_p^x B_q^y \frac{c}{j8\pi^2 L \cos\bar{\phi}_n} \exp(-2\pi f_{xc}\nu) \\ \cdot \{\exp(\pi F_x \nu)[I_2(K_1) - I_2(K_2)] \\ + \exp(-\pi F_x \nu)[I_2(K_3) - I_2(K_4)]\} \end{aligned} \tag{13}$$

where $I_2(K)$ and K_1, K_2, K_3, K_4 are defined in the Appendix.

As noted above, several approximations are made in arriving at (12) and (13). We compare this image-domain model to an image formed by applying the IDFT to a 128 × 128 array of polar-format samples given in (4). We assume 500-MHz bandwidth centered at 10 GHz and ± 1.4° aspect angle. The parameters chosen for this example are $L = 10$ m, $\alpha = 1$, $x = 11$ m, $y = 12$ m, $\bar{\phi} = 0.1°$, and $A = 1$. The relative error between the image-domain model and the image formed from the frequency-aspect domain data for this example is less than 1%.

Note that the transformation of the frequency-aspect model to the image domain is done for computational convenience and is not a requirement for estimation of the parameters of the 2-D scattering model in (4). In cases where the approximation error in (13) is unacceptably high or a different image formation algorithm is used, the frequency-aspect model is available for parameter estimation. Direct processing of raw radar data to produce features, rather than postprocessing images, has been suggested for fast detection of bright lines [17] and estimation of frequency-dependent scattering [8].

IV. Curve Fitting

In this section, we present an approximate maximum likelihood (ML) technique for estimating the parameters of the image-domain scattering model. For each of p scattering centers, there are eight real-valued parameters to be estimated: the amplitude and phase, A_n, frequency damping r_n, aspect damping γ_n, length L_n, tilt angle $\bar{\phi}_n$, down-range position x_n, and cross-range position y_n. For the case where $L \neq 0$, we require $\gamma_n = 0$, whereas $L = 0$ implies $\bar{\phi}_n$ is not estimated.

Use of the image-domain model requires knowledge of both the radar sensor and the image formation process. For example, for Fourier transform imaging [3], required parameters are center frequency, bandwidth, total angle span (aperture), numbers of frequency and angle samples, the data window functions used in down range and cross range and the image-domain sample spacing.

The initial step in our algorithm is to segment the image into small image chips, each of which contains a small number of scattering centers. Using the image domain model, a curve fit is then computed for each image chip. There exist automatic segmentation algorithms [18]; alternatively, the image can be segmented visually with human interaction. Whichever segmentation procedure is chosen, the result is a partitioning of the image into a set of smaller image chips, each of which contains very few scattering centers. The segmentation highlights an advantage of estimating parameters in the image domain: we partition the large problem of estimating a single parametric model of large order into smaller, more tractable problems that can be solved in parallel.

For each segmented image chip we estimate model parameters by minimizing the squared error between the model and the measured image domain data

$$J(\Theta) = \sum_{\text{pixels}} |\text{image chip} - \text{model}(\Theta)|^2 \tag{14}$$

where Θ is a vector containing the parameters to be estimated. An iterative optimization procedure is used to minimize (14). There are many nonconvex optimization procedures in the literature, and we choose to use the simplex downhill method [19]. The simplex method is desirable because it is numerically stable and does not require a gradient or Hessian of the cost function.

The least-squares cost function in (14) is nonconvex with many local minima. Therefore, parameter initialization and model-order selection [20] are very important. Presently, model order selection and the detection of $L \neq 0$ is performed interactively by a human user or with automated, *ad hoc* image-processing criteria [21]. Likewise, L_n and $\bar{\phi}_n$ are initialized by the user. Initialization of range and cross-range positions is computed from local maxima in the image chip, while r_n and γ_n are initialized at zero (isotropic point scattering). For a fixed parameter set Θ, the least-squares cost function J is quadratic in the complex amplitude parameter A; therefore, the least-squares estimate of A is computed noniteratively using a matrix pseudo-inverse.

At convergence, the simplex downhill optimization yields estimates of scattering parameters that describe the position, size, shape, and orientation of the scattering centers that comprise the measured target. Automation of model order selection and parameter initialization is a topic of continuing development, both for our proposed scattering model and for simpler point scattering models [21], [22].

V. EXAMPLES

We present two examples to illustrate the fidelity of the scattering model and the accuracy of the estimation procedure. The estimation algorithm extracts parameters that describe the position, shape, and orientation of the scattering centers on the target. The estimation results show that the physically based scattering model provides an excellent means for compressing a large, measured data record into a small set of physically relevant parameters. Measurements were collected at The Ohio State University ElectroScience Laboratory (ESL) Compact Range [23].

First, we consider the scattering from a square flat plate. We analyze stepped frequency measurements of the plate for frequencies 9.5–10.5 GHz in 20-MHz steps and for angles $\pm 3^\circ$ (in 0.5° steps) from broadside to one of the edges. The plate is a two foot square and lies in the plane of rotation. The measurement polarization is horizontal.

Fig. 1 shows an image of the plate. The image contains three scattering centers. The broadside response of the edge of the plate appears as a line in the image. The two corners on the back of the plate appear as localized scattering mechanisms. These three mechanisms are segmented in the image and the algorithm of Section IV is used to estimate the parameters. Table III shows the estimated parameters and their actual values. The actual values are based on the assumption that the plate is exactly two foot square and is perfectly aligned during radar measurements so that 0 corresponds to broadside to an edge. The estimated tilt angle is approximately -0.6°, which is an indication that the plate was not exactly aligned with 0° broadside to the radar. Fig. 2 shows the amplitude of the scattering from the plate as a function of angle at the center frequency 10 GHz. Note that the peak is not at 0° as we would expect for a perfectly aligned target. The misalignment of the target also contributes to a small amount of error in the expected locations of the three scattering centers.

The image generated with the estimated parameters has less than 3% mean-square error (MSE) with the measured image. The error in the estimated location of the individual scattering centers is small and in each case is less than one tenth the Fourier resolution. The geometric type (α) estimates correctly identify the edge specular and corner diffraction scattering behaviors. The algorithm compresses the measured, complex-valued 51×13 point data array into a small table of seven numbers describing the edge mechanism and six numbers

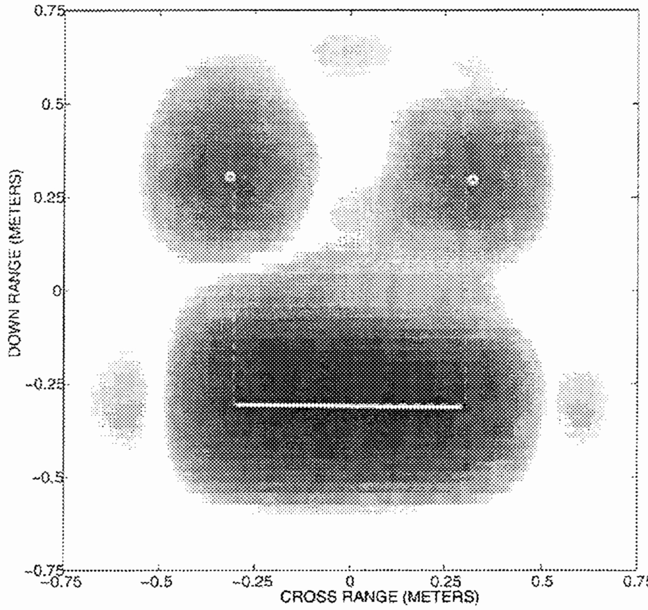

Fig. 1. Image and estimates for plate example.

TABLE III
ESTIMATED SCATTERING PARAMETERS FOR PLATE EXAMPLE; FOURIER RESOLUTION IS 30 cm

Scatterer	Attribute	Estimated	Actual
Front Edge	length	0.5920m	.6096m
	tilt	$-0.6567°$	0
	down range	-0.3085m	-0.3048m
	cross range	-0.0014m	0.0000m
	alpha	0	0
Back Left Corner	down range	0.3048m	0.3048m
	cross range	-0.3157m	-0.3048m
	alpha	-1	-1
Back Right Corner	down range	0.2971m	0.3048m
	cross range	0.3216m	0.3048m
	alpha	-1	-1

describing each of the two corner mechanisms. The model, therefore, provides a 69 : 1 lossy compression of the original measured frequency-aspect data.

Second, we consider a scale model of an F117 aircraft. The model is constructed from flat aluminum plates. We analyze data from 9.5 to 10.5 GHz in 10-MHz steps and $\pm 3^\circ$ from normally incident on the leading edge of one of the wings in 0.1° steps. Fig. 3 shows the image of the aircraft with an overlay showing the true location of the target in the image plane. The alpha estimate for the wing edge is zero, which is consistent with the target geometry. Also, we fit two localized mechanisms to the tail region of the aircraft. The estimated locations of these scatterers are indicated by the small circles in the image. Table IV shows the parameter estimates for this example. The thick solid line that is nearly coincident with the leading edge of the wing shows the estimated location, tilt, and length of the scattering center. When considering all three scattering centers, the overall MSE in the image is less than 7%. The model provides a compression ratio of 648 : 1.

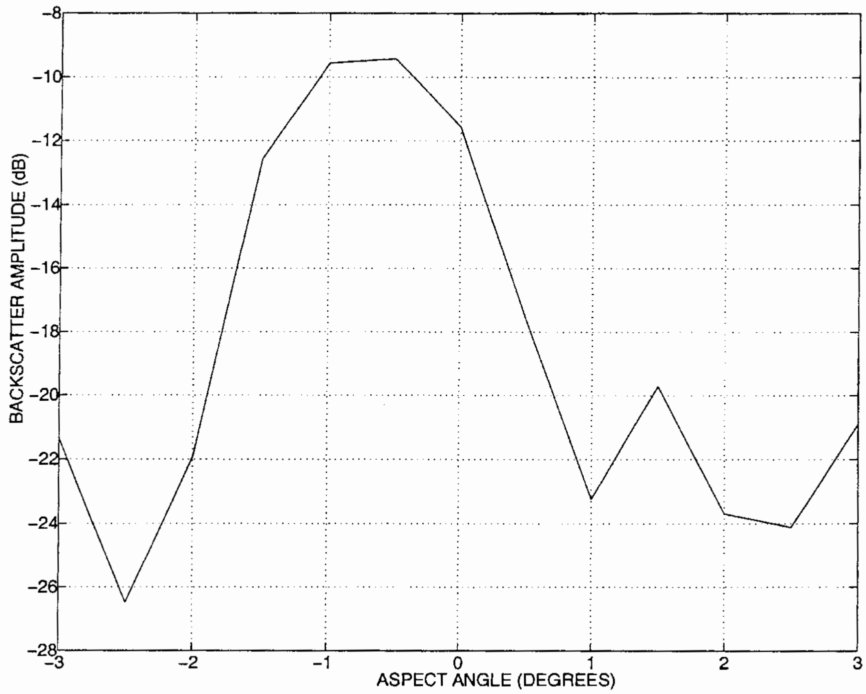

Fig. 2. Magnitude of plate scattering versus aspect angle indicating target misalignment (frequency 10 GHz).

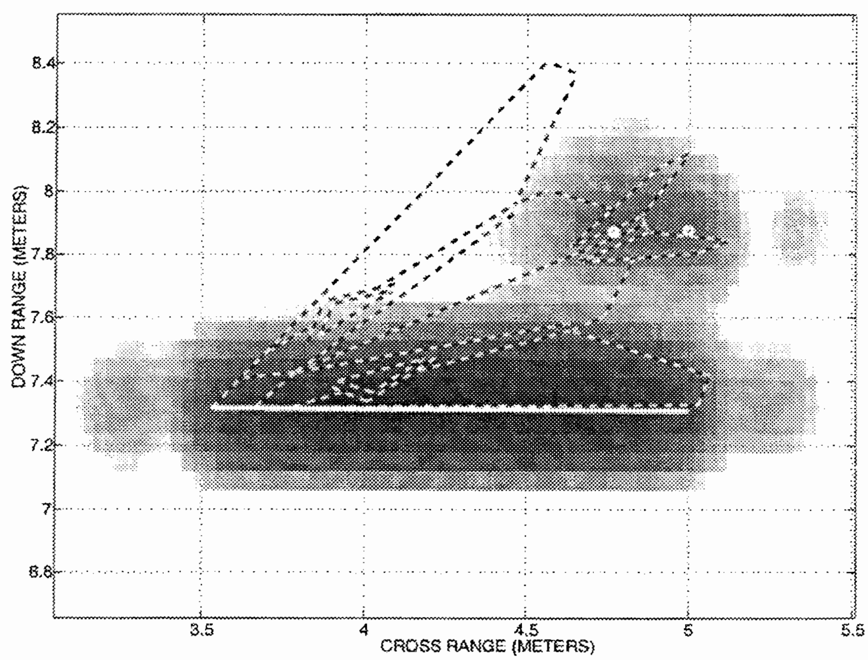

Fig. 3. Image of scale model F117 Aircraft with estimates of scattering centers using the distributed scattering model.

To illustrate the advantages of incorporating aspect dependence in our scattering model, we compare with a point scattering model. We use the localized scattering center model in (12), (with frequency and angle dispersion parameters r and γ and with $L = 0$) to fit the scattering from the leading edge of the aircraft wing. Model order is varied from one to six. Fig. 4 shows the results for a model order of four. The localized scattering center model requires a much larger set of parameters to achieve comparable MSE than the distributed scattering center ($L \neq 0$) model. Although a lower MSE is achieved for increasing model order (see Table V), using six or fewer points the localized scattering center model does not achieve the MSE of the proposed distributed scattering model. For example, a model order of six corresponds to a table of 36 numbers describing the scattering and, in this example, yields a MSE greater than 11%. A further disadvantage of the localized scattering center model for describing distributed scattering is that the estimated locations are not related to any physical quantity.

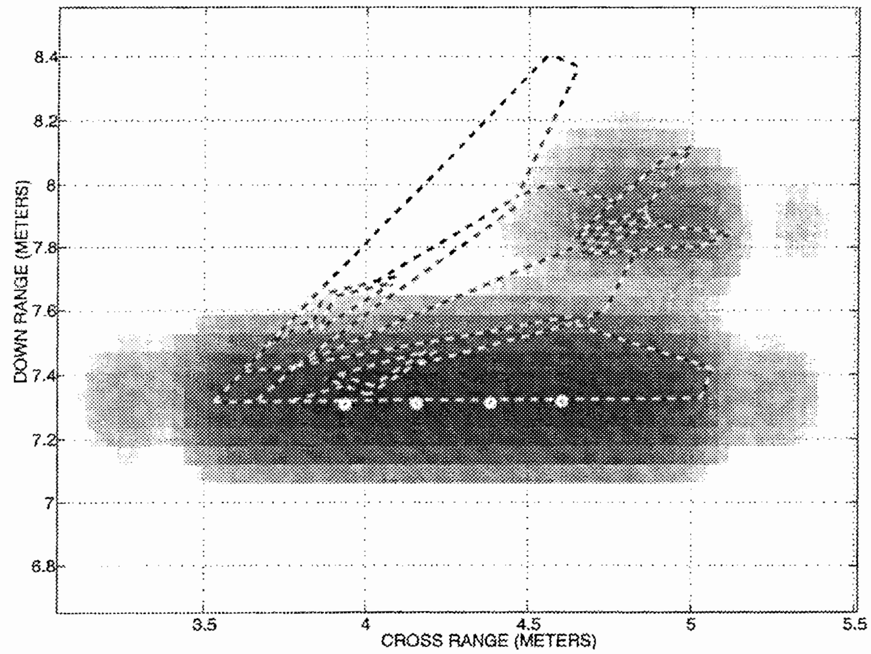

Fig. 4. Image of scale model F117 Aircraft with estimates of wing edge using the localized scattering model (model order 4).

TABLE IV
ESTIMATED SCATTERING PARAMETERS FOR F117 EXAMPLE (DISTRIBUTED SCATTERING MODEL)

Scatterer	Attribute	Estimate
Wing Edge	Length	1.4891m
	Tilt	−0.3651°
	Down Range	7.3127m
	Cross Range	4.2644m
	Alpha	0
Tail Region #1	Down Range	7.8733m
	Cross Range	4.7670m
	Alpha	-1
Tail Region #2	Down Range	7.8756m
	Cross Range	4.9986m
	Alpha	-2

TABLE V
MEAN SQUARE ERROR VERSUS MODEL ORDER FOR F117 EXAMPLE (LOCALIZED SCATTERING MODEL)

Model Order	Mean Square Error
1	89.97%
2	68.64%
3	50.57%
4	34.74%
5	21.82%
6	11.53%

VI. STATISTICAL ANALYSIS

In this section, we investigate the noise sensitivity of estimated parameters for the scattering model proposed in (4). We present theoretical predictions of estimation performance and compare theory to measurements of a flat plate. Specifically, we use the CRB to address two practical issues: the resolution limit for closely spaced scattering centers and the role of relative bandwidth in estimating the frequency dependence parameter, α.

The CRB for the model is derived in [16] and provides an algorithm-independent lower bound on the error variance for unbiased estimates of the model parameters. The derivation assumes the scattering model of (4) with an additive perturbation

$$E(f,\phi) = \sum_{n=1}^{p} E_n^s(f,\phi) + \eta(f,\phi). \tag{15}$$

Here, $\eta(k,\phi)$ represents the modeling error (background clutter, sensor noise, model mismatch, incomplete motion compensation, antenna calibration errors, etc.) and is assumed to be a white Gaussian noise process. For any choice of model parameters, the bound is computed by inversion of the information matrix [24]. We report signal-to-noise (SNR) values using the ratio of signal energy to noise energy computed for the frequency-aspect domain samples; interpretation of SNR in the image domain as a difference between peak signal level and clutter floor (i.e., after pulse compression) requires a shift of $10\log_{10} NM$ dB for a point scatterer (less for other types of scattering), where N and M are the number of frequency and aspect samples.

First, we consider resolution. For a given SNR of a single-point scatterer (SNR/mode), we define *resolution* as the minimum distance between two equal amplitude scattering centers resulting in nonoverlapping 95% confidence regions for the estimated locations [25]. Our definition is illustrated in Fig. 5. The figure is computed for 500-MHz bandwidth with $\pm 1.4°$ aperture and $f_c = 10$ GHz, consistent with the existing SAR sensor used for the MSTAR [26] data set. This bandwidth yields a Fourier resolution of 30 cm; windowing for sidelobe suppression results in coarser resolution. Further, we assume 64 equally spaced samples in both frequency and aspect. The SNR is -10 dB for the figure. The ellipses show the 95%

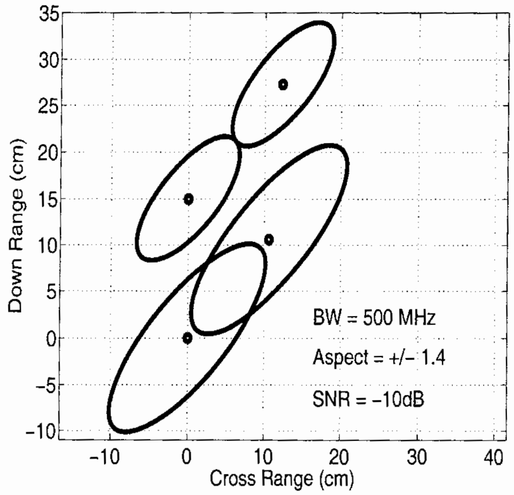

Fig. 5. Definition of resolution using 95% confidence ellipses.

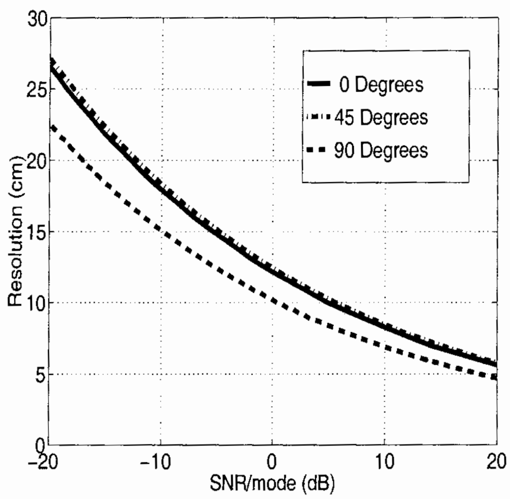

Fig. 6. Resolution versus SNR for three different orientations of two-point scatterers.

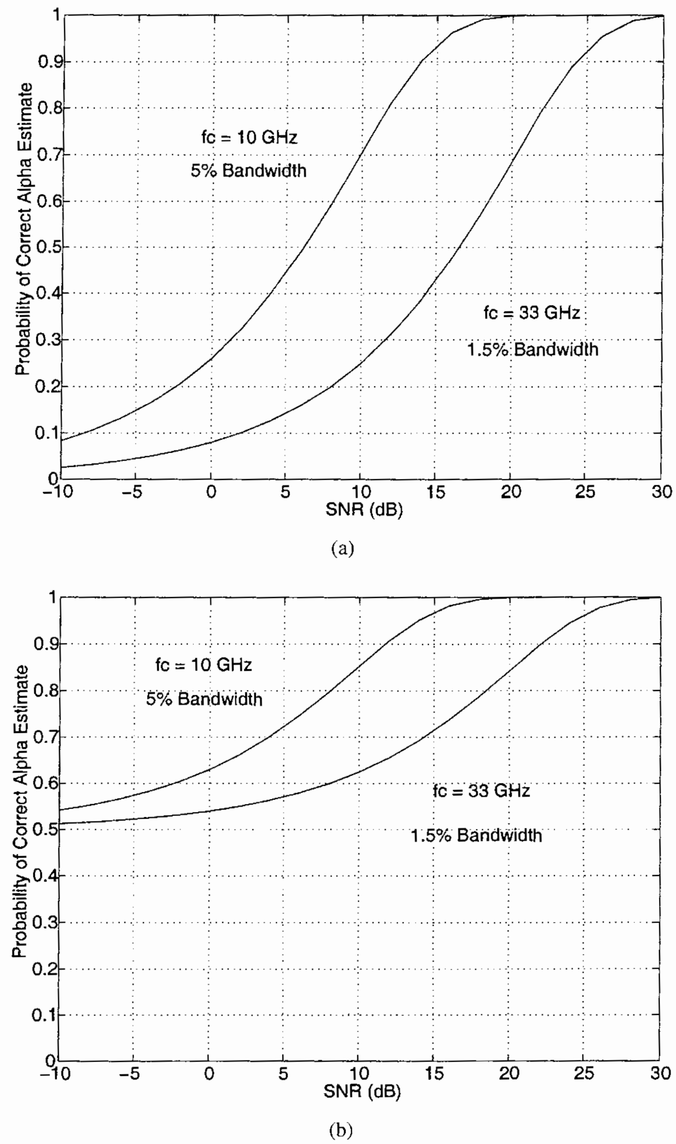

Fig. 7. Predicted probability of correctly identifyingalpha. (a) Five α values $\{-1, -0.5, 0, 0.5, 1\}$. (b) α $\frac{1}{2}$ versus 1.

confidence regions for the location estimates of four localized scatterers. The pair in the lower portion of the figure are not resolved since the ellipses overlap. The pair in the upper portion are, by definition, resolved since the confidence regions are disjoint.

Adopting this definition, resolution versus SNR/mode is shown in Fig. 6. The resolution depends on the orientation of the two point scatterers. The dashed line shows resolution for point scatterers separated an equal distance in both down range and cross range (i.e., aligned 45° to the aperture). The solid line and the dash-dot line show resolution for two-point scatterers aligned parallel and orthogonal to the aperture, respectively. For an SNR/mode of -4 dB, the limit of resolution achievable by model-based scattering analysis is below one-half the Fourier resolution; model-based resolution is limited by sensor bandwidth and SNR, which includes mismatch from the model in (15).

Second, we consider the effect of relative bandwidth and SNR in accurately detecting the frequency dependence parameter α for a single scattering mechanism. We characterize performance limits by assuming a parameter estimator that is unbiased, statistically efficient [24] and normally distributed (as is asymptotically true for the least-squares estimator). Fig. 7(a) shows the probability of correct detection of the discrete-valued α parameter versus SNR for 1 ft resolution X-band and K-band SAR systems. The X-band data are as specified above; the K-band data are for 500-MHz bandwidth, $\pm 0.4242°$ aperture, and $f_c = 33$ GHz, consistent with a Lincoln Laboratory sensor [27]. The analytically derived detection results are averaged over five scattering types ($\alpha \in \{-1, -\frac{1}{2}, 0, \frac{1}{2}, 1\}$). Notably, uncertainty in estimating α decreases drastically with an increase in relative bandwidth. This finding reaffirms the one-dimensional results in [2] and [13] that accurate estimation of the trend in scattering amplitude versus frequency requires either high bandwidth or low noise power. In Fig. 7(b) the detection of α is restricted to the binary hypotheses of $\alpha = \frac{1}{2}$ or $\alpha = 1$; this represents, for $L \neq 0$, the scenario of distinguishing a cylinder from a dihedral.

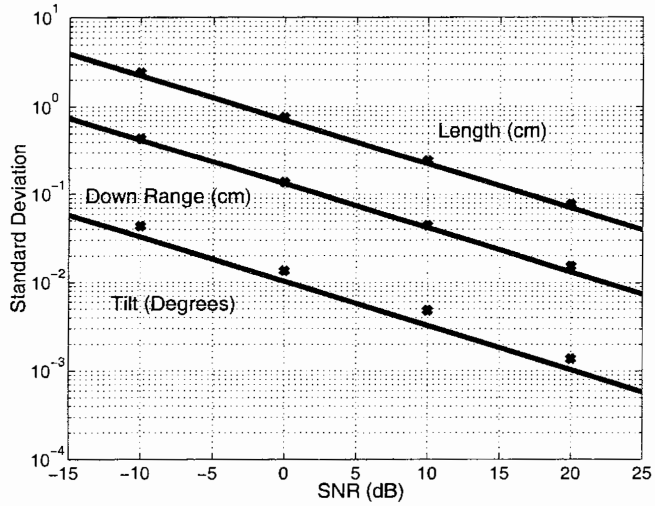

Fig. 8. Parameter uncertainty versus SNR for scattering model $L \neq 0$. The points indicate observed error variance using our estimation algorithm.

To compare theoretical predictions with measurements, we consider the edge-scattering example from Fig. 1. The CRB's are compared to the parameter estimation variance observed using measured data. In Fig. 8 we show the lower bound for standard deviation of parameter estimates versus SNR for the plate edge seen in Fig. 1. The bounds on standard deviation are computed using the frequency and angle spans described for Fig. 1 and the actual parameters in Table III, with the exception of tilt, for which the true parameter is assumed to be $\bar{\phi} = -0.6567°$. For four values of SNR, synthetic noise is added to the measured data, and parameters are estimated for 100 noise trials. The observed standard deviation in the estimated parameters is shown in Fig. 8 by overlaid crosses. Note that the observed estimation error variance is near the bound for the values of SNR considered. This implies that our suboptimal estimation algorithm is nearly statistically efficient and that the CRB can be useful as a predictor of parameter uncertainty.

A CRB prediction of error variance is a tractable tool that assumes an additive white Gaussian behavior for clutter and modeling error and assumes the estimator achieves the bound. Yet, from Fig. 8 we observe that the analysis nonetheless provides a reasonable prediction of experimentally observed error variance. As such, the bound is a useful guide for both evaluating performance-versus-computation tradeoffs in algorithm design and investigating the uncertainty in the estimated parameters as a function of system parameters such as bandwidth and center frequency.

VII. Conclusion

We present a parametric scattering model for the extraction of scattering centers from radar data measured as a function of frequency and aspect angle. The scattering model balances physical fidelity with simplicity in functional form to yield both smaller modeling error and a richer description of scattering behavior when compared to either Fourier imaging or point scattering models. Data analysis using the proposed model has application to feature extraction for target identification, SAR data compression, and scattering studies. The model is developed in the frequency-aspect domain and is motivated by GTD-based and physical optics scattering principles. We present an image-domain algorithm for estimating model parameters and thereby gain both clutter suppression and computational savings. We use the CRB as a tool for predicting uncertainty in estimated parameters. The scattering model and the image-domain estimation algorithm are demonstrated in three measured data examples.

Appendix

$$
\begin{aligned}
I_2(K) = {} & -j\cot\bar{\phi}_n \exp\Bigg(-K\cot\bar{\phi}_n\Bigg(r_n + j\Bigg(\Bigg(\frac{2x}{c} \\
& - \beta_p^x - t_x\Bigg) + \tan\bar{\phi}_n\Bigg(\frac{2y}{c} - \beta_q^y - t_y\Bigg)\Bigg)\Bigg)\Bigg) \\
& \times \big(j2\pi \operatorname{sgn}(K)\operatorname{sgn}(-Kr_n\cot\bar{\phi}_n) \\
& \times \operatorname{rect}_{\frac{L\cos\bar{\phi}_n}{c}}\Bigg(\cot\bar{\phi}_n\Bigg(t_x - \frac{2x}{c} + \beta_p^x\Bigg)\Bigg) \\
& + E_1\Bigg(-Kr_n\cot\bar{\phi}_n - jK\Bigg(\cot\bar{\phi}_n\Bigg(\frac{2x}{c} - \beta^x - t_x\Bigg) \\
& - \frac{L\cos\bar{\phi}_n}{c}\Bigg)\Bigg) - E_1\big(-Kr_n\cot\bar{\phi}_n - jK \\
& \times \Bigg(\cot\bar{\phi}_n\Bigg(\frac{2x}{c} - \beta^x - t_x\Bigg) + \frac{L\cos\bar{\phi}_n}{c}\Bigg)\Bigg)\Bigg) \\
& + j\pi \operatorname{sgn}(K)\operatorname{rect}_{\frac{L\cos\bar{\phi}_n}{c}}\Bigg(t_y - \frac{2y}{c} + \beta^y\Bigg) \\
& + E_1\Bigg(-jK\Bigg(t_y - \frac{2y}{c} + \beta^y - \frac{L\cos\bar{\phi}_n}{c}\Bigg)\Bigg) \\
& - E_1\Bigg(-jK\Bigg(t_y - \frac{2y}{c} + \beta^y + \frac{L\cos\bar{\phi}_n}{c}\Bigg)\Bigg)
\end{aligned}
$$

where

$$
\begin{aligned}
K_1 &= 2\pi(f_{y2} - f_{x1}\tan\bar{\phi}_n) \\
K_2 &= 2\pi(f_{y1} - f_{x1}\tan\bar{\phi}_n) \\
K_3 &= 2\pi(f_{y1} - f_{x2}\tan\bar{\phi}_n) \\
K_4 &= 2\pi(f_{y2} - f_{x2}\tan\bar{\phi}_n) \\
\nu &= r_n + j\Bigg\{\frac{2x_n}{c} - \beta_p^x - t_x \\
&\quad - \tan\bar{\phi}_n\Bigg(t_y - \frac{2y_n}{c} + \beta_q^y\Bigg)\Bigg\} \\
\operatorname{rect}_T(x) &= \begin{cases} 1, & -T/2 \le x \le T/2 \\ 0, & \text{otherwise} \end{cases} \\
E_1(z) &= \int_z^{\infty} \frac{\exp(-t)}{t}\, dt.
\end{aligned}
$$

Acknowledgment

The authors would like to thank J. Stach of the Environmental Research Institute of Michigan, Ann Arbor, for his support.

REFERENCES

[1] J. B. Keller, "Geometrical theory of diffraction," *J. Opt. Soc. Amer.*, vol. 52, pp. 116–130, 1962.

[2] L. C. Potter, D.-M. Chiang, R. Carriere, and M. J. Gerry, "A GTD-based parametric model for radar scattering," *IEEE Trans. Antennas Propagat.*, vol. 43, pp. 1058–1067, Oct. 1995.

[3] D. L. Mensa, *High-Resolution Radar Cross Section Imaging*. Boston, MA: Artech House, 1991.

[4] M.-W. Tu, I. J. Gupta, and E. K. Walton, "Application of maximum likelihood estimation to radar imaging," *IEEE Trans. Antennas Propagat.*, vol. 45, pp. 20–27, Jan. 1997.

[5] I. J. Gupta, "High-resolution radar imaging using 2-D linear prediction," *IEEE Trans. Antennas Propagat.*, vol. 42, pp. 31–37, Jan. 1994.

[6] J. J. Sacchini, "Development of two-dimensional parametric radar signal modeling and estimation techniques with application to target identification," Ph.D. dissertation, The Ohio State Univ., Columbus, 1992.

[7] R. Bhalla and H. Ling, "Three-dimensional scattering center extraction using shooting and bouncing ray technique," *IEEE Trans. Antennas Propagat.*, vol. 44, pp. 1445–1453, Nov. 1996.

[8] L. C. Potter and R. L. Moses, "Attributed scattering centers for SAR ATR," *IEEE Trans. Image Processing*, vol. 6, pp. 79–91, Jan. 1997.

[9] Y. Hua, "High resolution imaging of continuously moving object using stepped frequency radar," *Signal Processing*, vol. 35, no. 1, pp. 33–40, Jan. 1994.

[10] R. G. Kouyoumjian and P. H. Pathak, "A uniform geometrical theory of diffraction for an edge in a perfectly conducting surface," *Proc. IEEE*, vol. 62, pp. 1448–1461, Nov. 1974.

[11] M. A. Plonus, R. Williams, and S. C. H. Wang, "Radar cross section of curved plates using geometrical and physical diffraction techniques," *IEEE Trans. Antennas Propagat.*, vol. AP-26, pp. 488–493, May 1978.

[12] R. A. Ross, "Radar cross section of rectangular flat plates as a function of aspect angle," *IEEE Trans. Antennas Propagat.*, vol. AP-14, pp. 329–335, May 1966.

[13] D.-M. Chiang, "Parametric signal processing techniques for model mismatch and mixed parameter estimation," Ph.D. dissertation, The Ohio State University, Columbus, 1995.

[14] D. C. Munson, J. D. O'Brian, and W. K. Jenkins, "A tomographic formulation of spotlight-mode synthetic aperture radar," *Proc. IEEE*, vol. 71, pp. 917–925, Aug. 1983.

[15] A. Dutt and V. Rohklin, "Fast fourier transforms for nonequispaced data II," *Appl. Computat. Harmonic Anal.*, vol. 2, no. 1, pp. 85–100, 1995.

[16] M. J. Gerry, "Two-dimensional inverse scattering based on the GTD model," Ph.D. dissertation, The Ohio State Univ., Columbus, 1997.

[17] G. Franceschetti, A. Iodice, and M. Tesauro, "From image processing to feature processing," *Signal Processing*, vol. 60, pp. 51–63, 1997.

[18] J. Stach and E. LeBaron, "Enhanced image editing by peak region segmentation," in *Proc. Antenna Meas. Tech. Assoc. 18th Symp.*, Seattle, WA, Sept. 1996, pp. 303–307.

[19] J. A. Nelder and R. Mead, "A simplex method for function minimization," *Computer J.*, vol. 7, pp. 308–313, 1965.

[20] A. Sabharwal and L. Potter, "Model selection for nested model classes with cost constraints," in *Proc. 9th IEEE Workshop Statistical Signal Array Processing*, Portland, OR, Sept. 1998, pp. 84–87.

[21] M. Koets, "Application of two-dimensional inverse scattering models to measured SAR imagery," M.S. thesis, The Ohio State Univ., Columbus, 1998.

[22] S. R. DeGraaf, "SAR imaging via modern 2-D spectral estimation methods," *IEEE Trans. Image Processing*, vol. 7, pp. 729–761, May 1998.

[23] E. K. Walton and J. D. Young, "The Ohio State University compact radar-cross section measurement range," *IEEE Trans. Antennas Propagat.*, vol. AP-32, pp. 1218–1223, Nov. 1984.

[24] H. L. Van Trees, *Detection, Estimation, and Modulation Theory—Part I*. New York: Wiley, 1968.

[25] M. P. Clark, "On the resolvability of normally distributed vector parameter estimates," *IEEE Trans. Signal Processing*, vol. 43, pp. 2975–2981, Dec. 1995.

[26] E. R. Keydel, S. W. Lee, and J. T. Moore, "MSTAR extended operating conditions: A tutorial," in *Conf. Algorithms Synthetic Aperture Radar Imagery III, Proc. SPIE*, Orlando, FL, Apr. 1996, pp. 228–242.

[27] L. M. Novak, G. J. Owirka, and C. M. Netishen, "Performance of a high-resolution polarimetric SAR automatic target recognition system," *Lincoln Lab. J.*, vol. 6, no. 1, pp. 11–24, 1993.

Michael J. Gerry was born in Burlington, VT. He received the B.S. degree in electrical engineering from the University of Delaware, Newark, in 1989, and the M.S. and the Ph.D. degrees in electrical engineering from The Ohio State University, Columbus, in 1993 and 1997, respectively.

From 1989 to 1991, he was with W. L. Gore & Associates in Newark, DE, working in the Electronic Products Division. From 1991 to 1997 he was a Graduate Research Associate at the ElectroScience Laboratory, Department of Electrical Engineering, The Ohio State University. Since September 1997 he has been with Synsis Corporation, DeWitt, NY, designing and developing secondary surveillance radar systems for air traffic control applications.

Lee C. Potter (S'89–M'90–SM'98) received the B.E. degree from Vanderbilt University, Nashville, TN, and the M.S. and Ph.D. degrees from the University of Illinois at Urbana-Champaign, all in electrical engineering.

Since 1991, he has been with the Department of Electrical Engineering at The Ohio State University, Columbus, where he is currently an Associate Professor. His research interests include statistical signal processing, inverse problems, detection, and estimation, with applications in radar target identification and ultrawide-band systems.

Dr. Potter is a 1993 recipient of the Ohio State College of Engineering MacQuigg Award for Outstanding Teaching.

Inder J. Gupta (S'80–M'82–SM'86) received the B.Sc. degree in electronics engineering from Panjab University, Chandiagarh, India, in 1975, the M.Tech. degree in electrical engineering from the Indian Institute of Technology, Kanpur, India, in 1977, and the Ph.D. degree in electrical engineering from The Ohio State University, Columbus, in 1982.

Since 1979, he has been working at The Ohio State University ElectroScience Laboratory where currently he is a Senior Research Scientist. His previous work experience includes Research Engineer at IIT Kanpur, India, and Graduate Research Associate at the University of Tennessee Space Institute, Tullahoma, TN. He has done extensive research on adaptive antenna systems and compact range measurement systems and has written several research articles in these areas. His current research interests include adaptive antenna arrays, electromagnetic scattering, compact range technology, radar imaging, and target recognition.

Dr. Gupta was the President of Antenna Measurement Techniques Association in 1997. He received IEEE Antennas and Propagation Society's H. A. Wheeler Applications Prize Paper Award in 1991. He is also the recipient of The Ohio State University College of Engineering Lumley Research Award for 1991 and 1998.

Andria van der Merwe was born in South Africa. She received the B.Ing. (*cum laude*) and M.Ing. degrees in electrical engineering from the University of Pretoria, South Africa. She is currently working toward the Ph.D. degree in electrical engineering at The Ohio State University, Columbus.

Her areas of interest include signal processing, optimization, detection and estimation, and electromagnetic scattering.